Nano Research

Open Access

Research Article

Porous amorphous ceramics enable confined growth of high-entropy spinel for high-temperature electromagnetic wave attenuation

Weichao Wang[1], Gu Liu[1] ✉, Liuying Wang[1] ✉, Jie Huang[1], Qiangqiang Wang[2], Qi Gu[1], Chaoqun Ge[1], Xiwei Yin[1], Shi Yan[1], and Renbing Wu[2] ✉

[1] *Rocket Force University of Engineering, Xi'an 710025, China*
[2] *College of Smart Materials and Future Energy, State Key Laboratory of Coatings for Advanced Equipment, Fudan University, Shanghai 200438, China*

Cite this article: *Nano Research*, **2026**, *19*, 94908670. https://doi.org/10.26599/NR.2026.94908670

ABSTRACT: Sustainable dielectric relaxation across a broad temperature window remains a significant challenge for high-temperature electromagnetic-wave (EMW) absorption, particularly in extreme conditions where dissipation pathways are severely constrained. Herein, a porous ceramic embedded with high-entropy nanocrystals (P-HEN) was developed by leveraging the confinement effect of the SiOCN covalent network. The confined growth and effective phase separation of $(FeNiCoAl)_3O_4$ nanocrystals generate thermally stable dielectric-relaxation activation units within the SiOCN matrix. Furthermore, the random distribution of multi-metal cations in the nanocrystals, together with the multi-interfacial interactions between the nanocrystals and the matrix, generates strong polarization responses. Consequently, P-HEN achieves sustained dielectric relaxation and full-band effective absorption in the X-band over a wide temperature range from 25 to 700 °C, while also exhibiting excellent thermal insulation and ablation resistance. This work demonstrates a confinement-enabled mechanism for stabilizing dielectric-relaxation loss at elevated temperatures, providing a new strategy for designing wide-temperature-window EMW absorbers.

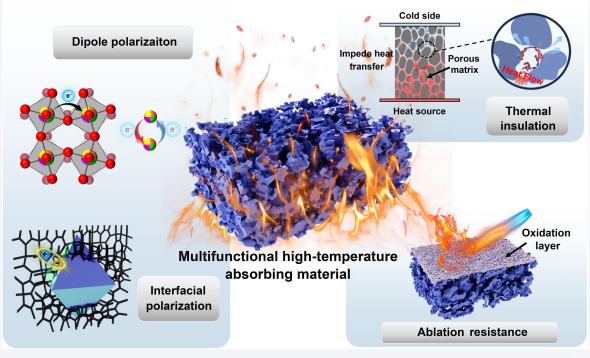

KEYWORDS: high-entropy, spinel, high-temperature, electromagnetic wave absorption

1 Introduction

To meet the long-term operational demands of crewed spacecraft, electronic devices, and other components in complex electromagnetic environments, the development of high-temperature electromagnetic wave (EMW) absorbers has become a critical area of research [1–3]. Unlike room-temperature absorbers that primarily emphasize "enhanced loss capability", high-temperature environment simultaneously imposes extreme boundary conditions, rendering the stability and tunability of electromagnetic responses at high temperatures decisive [4–7]. However, conventional high-temperature EMW absorbers still face several intrinsic limitations in high-temperature environments. For instance, some ceramic absorbers with high thermal stability often exhibit relatively weak dielectric responses due to their highly ordered lattice structures and limited defect density, resulting in insufficient attenuation capability and poor impedance matching [8–11]. In addition, many high-temperature EMW absorbing materials dominated by conductive loss are prone to carrier thermal excitation and interface barrier reconstruction in high-temperature environments, which further leads to significant drift in permittivity [12, 13]. These limitations highlight the urgent need to develop thermally robust EMW absorbers with intrinsically sustainable dielectric-relaxation mechanisms. Therefore, achieving sustainable and controllable dielectric relaxation and dissipation pathways in high-temperature environments is of critical significance for enabling effective EMW absorption across a wide temperature range.

SiOCN ceramics, characterized by a continuous Si–O/Si–C/Si–N covalent network and an amorphous nanostructure, exhibits excellent high-temperature resistance and is widely regarded as an ideal matrix for constructing high-temperature functional ceramics [14, 15]. However, the dielectric loss of typical SiOCN is often

Received: February 7, 2026; **Revised:** March 13, 2026
Accepted: March 20, 2026

✉Address correspondence to Gu Liu, liugu5032@163.com; Liuying Wang, lywangxa@163.com; Renbing Wu, rbwu@fudan.edu.cn

constrained by its "inert" covalent skeleton, resulting in an insufficient density of intrinsically sustainable dielectric relaxation and thereby limiting attenuation and impedance matching [16, 17]. In recent years, nano-interfacial modulation and entropy-increasing engineering have been demonstrated to markedly alleviate the insufficient dielectric relaxation [18, 19]. In particular, the formation of nanoscopic heterointerfaces can optimize gradients in permittivity and conductivity as well as barrier-layer structures, which is beneficial for establishing stable Maxwell–Wagner interface polarization and space-charge accumulation, thereby constructing a multichannel, synergistic energy-dissipation network [20–22].

Spinel-type oxides possess distinctive crystal-chemical tunability and rich charge-response mechanisms [23, 24]. Their structures are composed of a three-dimensional coordination framework built from A-site tetrahedra and B-site octahedra, intrinsically providing a structural basis for the coexistence of multivalent cations and reversible site-occupancy regulation, which facilitates multisource dielectric loss under an alternating electric field [25–27]. On the one hand, A/B-site occupancy disorder and the associated local coordination distortion give rise to pronounced local charge-density fluctuations and polarization inhomogeneity, thereby extending the relaxation time-constant distribution and enhancing polarization loss [28, 29]. On the other hand, the spinel phase features high structural tolerance and a broad solid-solution space, enabling the accommodation of diverse transition-metal cations while maintaining a stable lattice framework, which favors the formation of high-entropy configurations [30]. The multicomponent entropy-increased systems can induce local coordination environments and lattice distortion at the atomic scale, generating local charge fluctuations and polarization inhomogeneity, thereby increasing the density of defect/interfacial states and broadening the distribution of relaxation time constants [31, 32]. Therefore, high entropy spinel phases not only exhibit intrinsically favorable dielectric responses but can also serve as a designable "dielectric-activation building block" to provide EMW dissipation channels.

Herein, a porous ceramic containing high-entropy nanocrystals (P-HEN) was synthesized by leveraging the confinement effect of the SiOCN covalent network. The confinement and protective effects provided by the continuous SiOCN covalent network are proposed to enable persistent dielectric loss of $(FeNiCoAl)_3O_4$ nanocrystals at elevated temperatures. Benefiting from the robust covalent network as well as the persistent dielectric activation effects, P-HEN exhibits excellent thermal-insulation and ablation-resistance performance, offering a new design paradigm for high-temperature electromagnetic-wave absorbers.

2 Experimental

2.1 Synthesis of polymetallic PSZ precursor

Typically, aluminum chloride hexahydrate ($AlCl_3{\cdot}6H_2O$, Aladdin, China), cobalt chloride hexahydrate ($CoCl_2{\cdot}6H_2O$, Aladdin, China), iron(III) chloride hexahydrate ($FeCl_3{\cdot}6H_2O$, Aladdin, China), and nickel chloride hexahydrate ($NiCl_2{\cdot}6H_2O$, Aladdin, China) were added sequentially to N,N-dimethylformamide (DMF, Aladdin, China) under heating and stirring until complete dissolution of the metal salts, yielding a dark-green metal ligand solution. The molar ratio of Al:Co:Ni:Fe metal ions was fixed at 1:1:1:8, and the molar ratio of total metal ions to DMF was set to 0.4:10, 0.6:10, 0.8:10, and 1.0:10. The resulting metal ligand solution was then diluted with tetrahydrofuran (THF, Aladdin, China) using an equimolar amount relative to DMF. Subsequently, the metal ligand solution was mixed with the linear poly(methyl)silazane (PSZ, Zhonggui New Material Co., Ltd., China) in an anhydrous and anaerobic environment at a ratio of 10 g PSZ solution per 0.1 mol DMF and stirring was continued until no bubbles were observed.

2.2 Preparation of SiOCN porous ceramics containing $(FeNiCoAl)_3O_4$ nanocrystals

The obtained precursor solution was completely impregnated into melamine foam (MF, 16 g/cm^3, Zhengzhou FoamTech Nano Materials Co., LTD., China) through a vacuum impregnation process, which lasted for 0.5 h to remove the excess solvent. Subsequently, the green bodys were pyrolyzed at 1100 °C for 4 h under a nitrogen flow rate of 150 mL/min. The resulting ceramics were further annealed at 1100 °C for 6 h in an air atmosphere, thereby obtaining SiOCN porous ceramics containing high-entropy nanocrystals (P-HEN). The ceramic samples obtained with the molar ratios of total metal ions to DMF of 0.4:10, 0.6:10, 0.8:10 and 1.0:10 were named P-HEN-1, P-HEN-2, P-HEN-3, and P-HEN-4 respectively.

The detailed characterization methods are presented in the Electronic Supplementary Material (ESM).

3 Results and discussion

3.1 Preparation and morphological characterization

Based on the excellent high-temperature structural stability of SiOCN, a spatially confined environment is constructed to effectively suppress abnormal grain growth and phase separation behaviors. The in situ self-assembly mechanism of $(FeNiCoAl)_3O_4$ nanocrystals within the SiOCN ceramic matrix is schematically illustrated in Fig. 1(a). Initially, carbonyl oxygen functional groups in the solvent, acting as Lewis bases, coordinate with Fe^{3+}, Co^{2+}, Ni^{2+}, and Al^{3+} metal ions, progressively replacing water molecules and chloride ions in their hydrated coordination shells to form thermodynamically stable metal–DMF complexes (M–DMF) [33]. Subsequently, these M–DMF complexes are tightly coupled with the polymethylsilane molecular chain network through weak coordination interactions and hydrogen bonding, enabling a highly uniform dispersion and loading of multi-metal species within the precursor system. Furthermore, the polymethylsilane network loaded with M–DMF is introduced into a melamine foam skeleton for impregnation and curing, achieving controllable three-dimensional structural shaping. Finally, under thermally driven conditions, the metal ligands gradually dissociate and induce oxidative reconstruction reactions of the metal ions, leading to in situ nucleation within the SiOCN ceramic matrix. Benefiting from the spatial confinement effect provided by the SiOCN matrix, abnormal grain growth and phase separation are significantly suppressed, resulting in a SiOCN ceramic uniformly loaded with $(FeNiCoAl)_3O_4$ nanocrystals. Notably, the precursor undergoes direct pyrolytic conversion within the three-dimensional porous network, ultimately forming a macroscopically interconnected and structurally stable porous ceramic material. As shown in the Fig. 1(b), P-HEN exhibits a consistent shrinkage ratio (30.3% ± 0.2%) and excellent shape retention, thereby broadening its potential application scope.

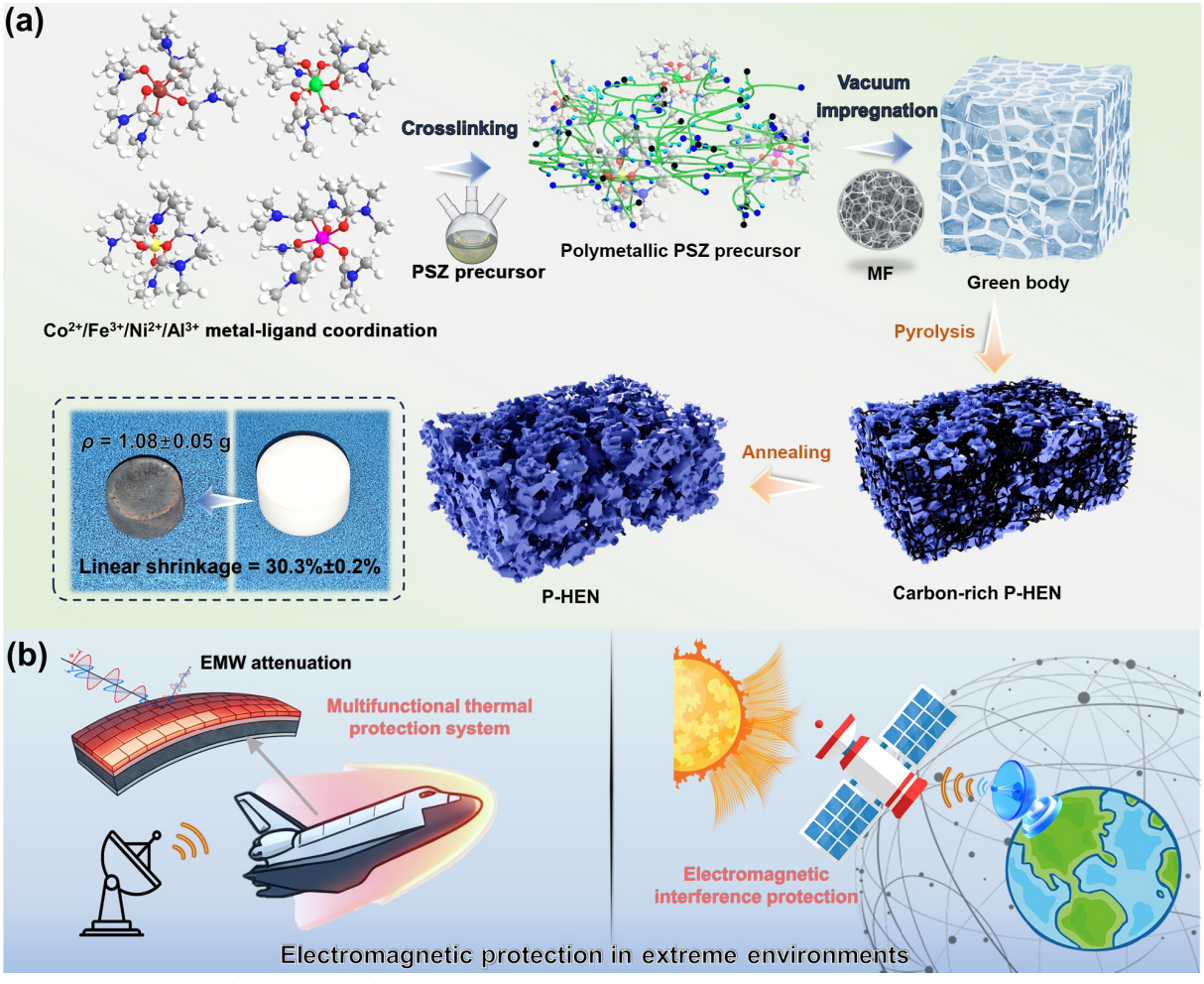

Figure 1 (a) Schematic illustration of the preparation of the P-HEN composite and (b) its application scenario for high-temperature EMW absorption.

The microstructural and chemical characterization results of the P-HEN provide evidence that $(FeNiCoAl)_3O_4$ nanocrystals were stably synthesized *in situ* within the SiOCN matrix and are highly uniformly dispersed. The scanning electron microscopy (SEM) images reveal that the P-HEN fully retains the three-dimensional porous foam architecture imparted by the MF template after pyrolysis, with abundant internal pore structures observed (Fig. 2(a)). The corresponding energy dispersive spectrometer (EDS) elemental mapping results confirm that the metallic elements are homogeneously distributed throughout the SiOCN matrix (Fig. S1 in the ESM). Such a structural configuration not only effectively reduces the density of the absorber but also enhances multiple scattering and prolonged propagation pathways of EMW. The confocal laser scanning microscopy (CLSM) images further confirm the formation of a ceramic network skeleton with non-uniform pore sizes (Fig. 2(b)). The spherical aberration-corrected transmission electron microscopy (AC-TEM) images of P-HEN provide evidence for the formation of nanocrystals. As shown in Figs. 2(c) and 2(d), the $(FeNiCoAl)_3O_4$ nanocrystals are uniformly dispersed and exhibit a distinct nanopolyhedral morphology, with an average particle size of 19.51 nm. To further investigate the atomic-scale crystal phase of the $(FeNiCoAl)_3O_4$ nanocrystals, high-angle annular dark-field scanning transmission electron microscopy (HAADF-STEM) was employed for atomic-resolution analysis. Figure 2(e) shows that the atomic arrangement of the nanocrystals exhibits a typical cubic spinel structure, in excellent agreement with the expected phase. The corresponding fast Fourier transform (FFT) pattern reveals that the diffraction spots along the [011] zone axis strictly obey the systematic extinction rules of the *Fd*-3*m* spinel structure, and no superstructure reflections are detected, indicating that multiple metal cations are randomly distributed over the crystallographic sites (Fig. 2(f)). Such an entropy-stabilized random occupancy configuration effectively suppresses ordering rearrangement and phase separation of multimetal cations under high-temperature conditions, thereby markedly improving the high-temperature structural stability of the composite system.

Figure 2(g) illustrates the site occupancy of Fe, Ni, Co, and Al atoms within the $(FeNiCoAl)_3O_4$ nanocrystals. At the initial stage of pyrolysis, Fe^{3+} ions, possessing the lowest nucleation barrier and the fastest diffusion kinetics, preferentially combine with oxygen to form Fe-O octahedral short-range ordered structures, which act as the core nucleation centers for crystal growth [34]. Subsequently, Al^{3+} ions, benefiting from their smaller ionic radius and strong preference for octahedral coordination, preferentially incorporate into the forming octahedral sites, thereby stabilizing the spinel framework [35, 36]. With further temperature elevation, Co^{2+} and Ni^{2+} ions gradually diffuse within the confined SiOCN matrix and participate in lattice growth. Among them, Co^{2+} ions, owing to their high coordination flexibility, can occupy both tetrahedral sites and partial octahedral sites, whereas Ni^{2+} ions, limited by relatively

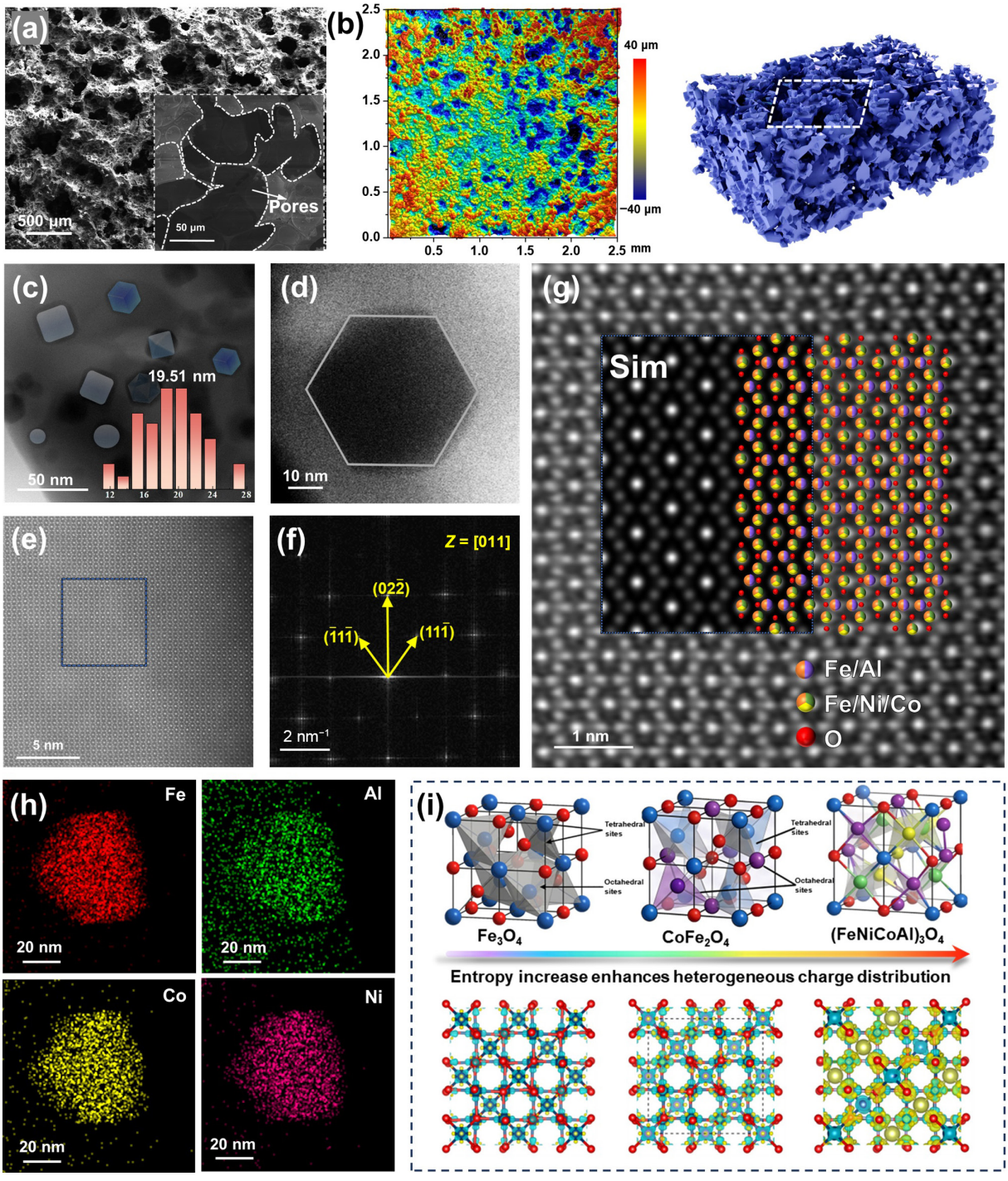

Figure 2 (a) SEM image, (b) CLSM image and schematic diagram of structure of porous structure on surface for SiOCN/HMO composite. (c)–(e) AC-TEM images of P-HEN. (f) FFT pattern of the AC-TEM image. (g) Atomic site occupancy map of $(FeNiCoAl)_3O_4$ nanocrystals. (h) Corresponding elemental maps of $(FeNiCoAl)_3O_4$ nanocrystal. (i) Differential charge density distributions of Fe_3O_4, $CoFe_2O_4$, and the multicomponent spinel $(FeNiCoAl)_3O_4$.

slower nucleation and diffusion kinetics, mainly enter the lattice at the later stage of crystallization [37]. Meanwhile, under an inert atmosphere and the reductive effect of residual carbon, a portion of Fe^{3+} ions is reduced to Fe^{2+} and preferentially occupies tetrahedral sites, thereby completing the filling of A sites in the spinel structure. Consequently, $(FeNiCoAl)_3O_4$ nanocrystals are formed with Fe^{3+} and Al^{3+} occupying octahedral sites, while Fe^{2+}, Co^{2+}, and Ni^{2+} occupy tetrahedral sites.

Such random occupancy of multimetal cations introduces pronounced local charge distribution inhomogeneity and polarization non-uniformity at the crystal scale, providing the SiOCN ceramic matrix with stable and highly dispersed dielectric response units, which are favorable for the introduction and synergistic enhancement of multiple dielectric polarization mechanisms [38]. Figure S2 in the ESM shows the geometric phase analysis (GPA) results obtained from HAADF-STEM. The strain distribution in this multicomponent spinel structure exhibits evident anisotropic characteristics, with significantly enhanced ε_{xx}

and ε_{yx} components. This indicates asymmetric stretching and compression of octahedra along specific crystallographic directions, inducing off-center displacement of B-site cations relative to the oxygen framework and thereby generating stable electric dipole moments. In contrast, the ε_{yy} and ε_{xy} components are relatively small, suggesting that lattice distortion is dominated by elastic strain rather than defect-induced effects, which confirms the high crystallinity of the $(FeNiCoAl)_3O_4$ nanocrystals and is beneficial for maintaining stable polarization states under high-temperature conditions. The EDS results further verify the uniform distribution and successful incorporation of Fe, Al, Co, and Ni elements within the nanocrystals (Fig. 2(h) and Fig. S3 in the ESM).

To further elucidate the electronic structure modulation and local bonding environment variation induced by multication occupation, the crystal structures of Fe_3O_4, $CoFe_2O_4$, and the multicomponent spinel $(FeNiCoAl)_3O_4$ are constructed (Fig. S4 in the ESM). The differential charge density distributions of the three structures are presented in Fig. 2(i). It can be clearly observed that with increasing compositional complexity and entropy effect, the polarization region surrounding the O atoms expands significantly, indicating pronounced electron accumulation around oxygen atoms. This phenomenon is particularly evident in the $(FeNiCoAl)_3O_4$ system. Meanwhile, the electron cloud distribution around the metal atoms becomes progressively asymmetric, accompanied by increased electronic disorder. These results suggest that the entropy-driven multication configuration introduces more abundant local polarization centers and charge redistribution pathways, thereby enhancing the polarization capability of the system. Furthermore, the density of states (DOS) of $(FeNiCoAl)_3O_4$ reveals that the electronic states near the Fermi level are primarily contributed by Fe 3d orbitals, with additional participation from Ni 3d and Co 3d states (Fig. S5 in the ESM). In the valence band region, a strong overlap between O 2p states and transition-metal 3d states is observed, indicating pronounced transition-metal–oxygen orbital hybridization. These results demonstrate that the Fe/Ni/Co–O sublattice serves as the main electronically active framework in this multicomponent spinel system. The cooperative contribution of multiple transition-metal d orbitals to the band-edge electronic states leads to a more complex electronic structure near the Fermi level. Such a multication configuration facilitates the formation of diverse local polarization centers and charge redistribution channels, thereby forming dielectric relaxation activation units in $(FeNiCoAl)_3O_4$.

To further verify the formation of $(FeNiCoAl)_3O_4$ within the SiOCN matrix and its phase stability at elevated temperatures, *in situ* heating X-ray diffraction (XRD) measurements were performed on the P-HEN over the temperature range of 25–1000 °C. As shown in Fig. 3(a), in addition to the clearly identifiable diffraction peaks corresponding to $(FeNiCoAl)_3O_4$, characteristic diffraction signals of SiO_2 are observed at room temperature, which is a commonly crystallized secondary phase in SiOCN systems. With increasing temperature, the diffraction peaks of $(FeNiCoAl)_3O_4$ exhibit only a slight shift toward lower diffraction angles, without the emergence of new phases or pronounced peak broadening or degradation. This behavior indicates that, under the encapsulation and confinement effect of the SiOCN matrix, the spinel phase retains its structural integrity even at high temperatures. The leftward shift of the diffraction peaks can be primarily attributed to thermally induced lattice expansion, leading to an increase in lattice parameters, which demonstrates the excellent thermal stability of the lattice structure. The high-temperature structural stability of the P-HEN is conducive to stabilizing dielectric-relaxation-related activated units over a wide temperature window, thereby sustaining the synergistic regulation and continuous contribution of multiple polarization relaxation processes.

Furthermore, the fourier transform infrared spectroscopy (FT-

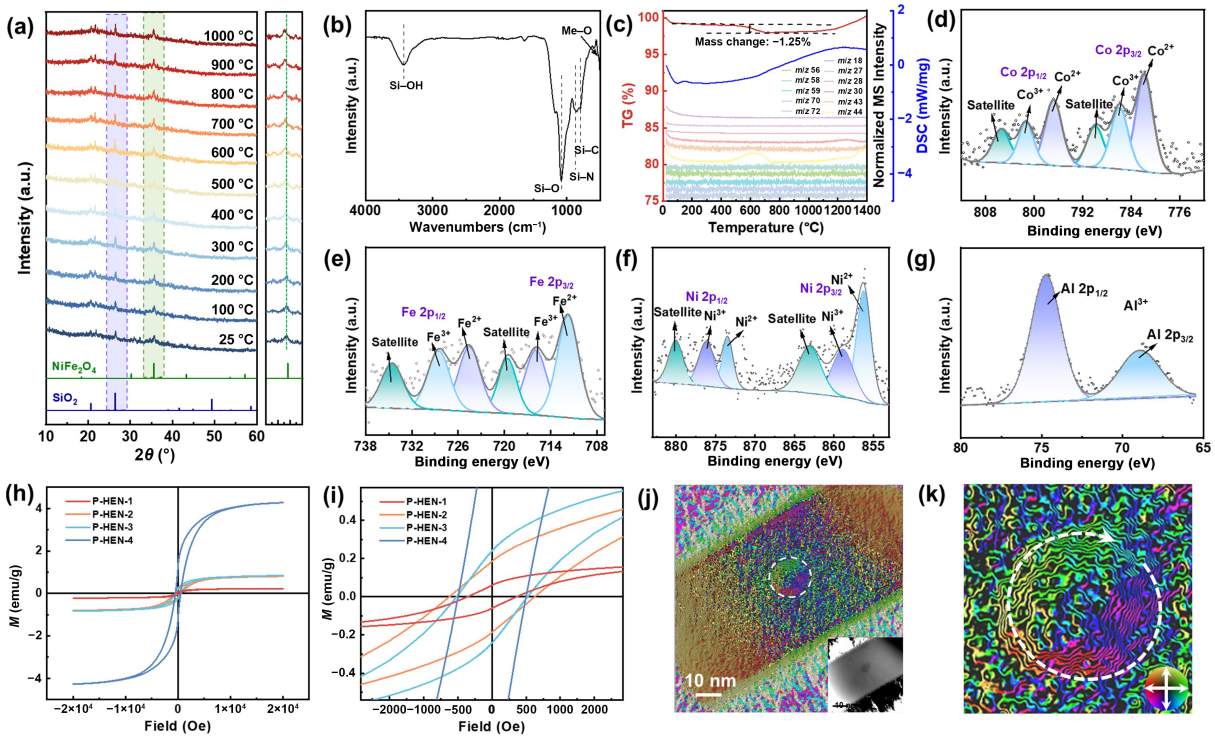

Figure 3 (a) High-temperature XRD patterns, (b) the FT-IR spectrum, and (c) TG-MS curves of P-HEN. High-resolution XPS spectra of (d) Co 2p, (e) Fe 2p, (f) Ni 2p, and (g) Al 2p. (h) and (i) Magnetic hysteresis loops of P-HEN with different $(FeNiCoAl)_3O_4$ loadings. (j) and (k) Holograms of P-HEN.

IR) was employed to analyze the bonding configurations of the composite. As shown in Fig. 3(b), the absorption bands located at 1086, 869, and 799 cm^{-1} correspond to the vibrational modes of Si–O, Si–N, and Si–C bonds, respectively, which are consistent with the typical chemical structure of the SiOCN matrix. In addition to these characteristic bands, a broad absorption feature appearing around ~ 500 cm^{-1} is associated with metal–oxygen vibrations and can be assigned as the fingerprint signal of the $(FeNiCoAl)_3O_4$ phase. The thermogravimetry–mass spectrometry (TG–MS) curves indicate that P-HEN exhibits excellent oxidation resistance and chemical stability (Fig. 3(c)). When heated in air up to 1400 °C, the mass change is only 1.25%. The variation in heat-flow signal is mainly associated with CO_2 (m/z = 44) release from the amorphous SiOCN matrix. To further elucidate the chemical bonding states and valence information, X-ray photoelectron spectroscopy (XPS) analysis was conducted. The XPS survey spectrum (Fig. S6 in the ESM) reveals the presence of Si 1s, O 1s, C 1s, N 1s, as well as Co 2p, Fe 2p, Ni 2p, and Al 2p signals, confirming the successful incorporation and effective coupling of the multimetal oxide phase with the SiOCN matrix. High-resolution spectra of Si 1s, O 1s, C 1s, and N 1s (Fig. S7 in the ESM) indicate that a covalently bonded network composed of Si–O, Si–C, Si–N, together with C–C and C–N bonds, is constructed within the material, thereby forming a robust SiOCN ceramic framework. In addition, the high-resolution XPS spectra of Co 2p, Fe 2p, Ni 2p, and Al 2p are presented in Figs. 3(d)–3(g). In the Co 2p spectrum, distinct Co $2p_{3/2}$, Co $2p_{1/2}$, and corresponding satellite peaks can be resolved, and peak deconvolution reveals the coexistence of Co^{2+} (782.0 and 796.9 eV) and Co^{3+} (786.1 and 801.5 eV). Similarly, the fitted Fe 2p spectrum indicates the simultaneous presence of Fe^{2+} (711.8 and 724.6 eV) and Fe^{3+} (715.9 and 728.4 eV), while the Ni 2p spectrum confirms the coexistence of Ni^{2+} (856.2 and 873.5 eV) and Ni^{3+} (858.9 and 876.1 eV). Meanwhile, characteristic signals corresponding to Al^{3+} (69.1 and 74.7 eV) are observed in the Al 2p spectrum [39]. As Al^{3+} preferentially occupies the A sites in the cubic spinel structure, adjustments in its local coordination environment and electron cloud distribution occur, resulting in a relative shift of the binding energy toward lower values, which is consistent with its structural site occupancy [40, 41]. Consequently, a P-HEN with excellent high-temperature phase stability is successfully synthesized. In addition, the magnetic hysteresis loops reveal that the P-HEN exhibit relatively weak magnetic behavior, and the overall variation trend is consistent with the $(FeNiCoAl)_3O_4$ filling concentration (Figs. 3(h) and 3(i)).

To further elucidate the dielectric response and relaxation activation effects of $(FeNiCoAl)_3O_4$ nanocrystals within the SiOCN matrix, off-axis electron holography was employed to characterize their local electric field distribution (Figs. 3(j) and 3(k)). The results demonstrate that a significant disturbance in the phase distribution of the electron beam occurs near the $(FeNiCoAl)_3O_4$ nanocrystals, accompanied by a noticeable deflection of the electron beam trajectory. This indicates the presence of a pronounced local potential gradient and electric field modulation effect surrounding the nanocrystals. Such a local field disturbs the propagation path and phase of the incident electromagnetic wave, thereby enhancing interfacial polarization and dielectric relaxation-related losses, which facilitates effective dissipation of electromagnetic energy. In contrast, no obvious phase deflection or electric field response was observed in the pure SiOCN matrix region, suggesting a limited intrinsic dielectric activation contribution. Therefore, the highly dispersed $(FeNiCoAl)_3O_4$ nanocrystals, effectively confined by the matrix, serve as critical dielectric relaxation activation units. Through their induced local field enhancement and interfacial polarization effects, they promote the synergistic relaxation processes of multiple polarization mechanisms in the P-HEN, thereby improving the overall dielectric loss capability and electromagnetic attenuation efficiency.

3.2 Temperature-dependent EMW absorption properties of SiOCN/HMO composite

As dielectric-relaxation activation units embedded in the SiOCN ceramic matrix, $(FeNiCoAl)_3O_4$ nanocrystals exert a pronounced influence on the dielectric response of P-HEN as a function of their loading concentration. The real (ε') and imaginary (ε'') parts of the complex permittivity are key parameters for characterizing dielectric-relaxation behavior [42, 43]. As shown in Fig. 4(a), with increasing filling concentration of the dielectric activation units, i.e., $(FeNiCoAl)_3O_4$ nanocrystals, both ε' and ε'' increase monotonically, indicating a concurrent enhancement in polarization capability and dielectric loss of the composite system. In addition, the relatively low real (μ') and imaginary (μ'') parts of the complex permeability indicate that P-HEN exhibits weak magnetic loss capability, making it difficult to effectively attenuate EMW through magnetic loss mechanisms (Fig. S8 in the ESM). Based on the reflection loss (RL) calculation (Note S2 in the ESM), the effective absorption bandwidth (EAB) of the P-HEN exhibits an obvious evolution with increasing $(FeNiCoAl)_3O_4$ nanocrystal loading at an identical thickness. Notably, P-HEN-3 delivers an EAB of up to 4.2 GHz, which covers the X band (Fig. 4(b)). Further evaluation of the RL of P-HEN-3 at different thicknesses reveals that, when the thickness falls within 3.5–4.0 mm, the EAB can fully cover the entire X band, demonstrating favorable thickness adaptability (Fig. 4(c)).

To verify the high-temperature stability of $(FeNiCoAl)_3O_4$ nanocrystals as dielectric-relaxation activation units, the in situ high-temperature electromagnetic parameters of the P-HEN were measured over 300–1073 K. The results indicate that, benefiting from the effective protection afforded by the SiOCN matrix, the $(FeNiCoAl)_3O_4$ nanocrystals remain dielectrically active across a broad temperature window, thereby endowing all samples with an overall high stability of electromagnetic parameters (Fig. 4(d) and Figs. S9–S11 in the ESM). To further elucidate the temperature-dependent dielectric relaxation contribution of $(FeNiCoAl)_3O_4$ nanocrystals within the composite system, the temperature-dependent DC conductivity of P-HEN-3 was measured using a Physical Property Measurement System (Fig. S12 in the ESM). Benefiting from the dielectric network formed by $(FeNiCoAl)_3O_4$ nanocrystals within the SiOCN ceramic, the DC conductivity of P-HEN-3 exhibits a pronounced transition from insulating to semiconducting behavior with increasing temperature, indicating that elevated temperatures facilitate the gradual formation of a quasi-percolation network. Furthermore, based on Debye relaxation theory, the conductive loss (ε_c') and polarization loss components (ε_p') at different temperatures were quantitatively analyzed (Figs. 4(e) and 4(f)). The results indicate that at low temperatures, polarization loss is the dominant form of dielectric loss in P-HEN. This observation confirming that localized charge-distribution inhomogeneity and polarization non-uniformity induced at the crystalline scale by the entropy-increase effect strengthen dipolar polarization loss. Meanwhile, the propagation of EMW across the interfaces between the nanocrystals and the SiOCN ceramic matrix

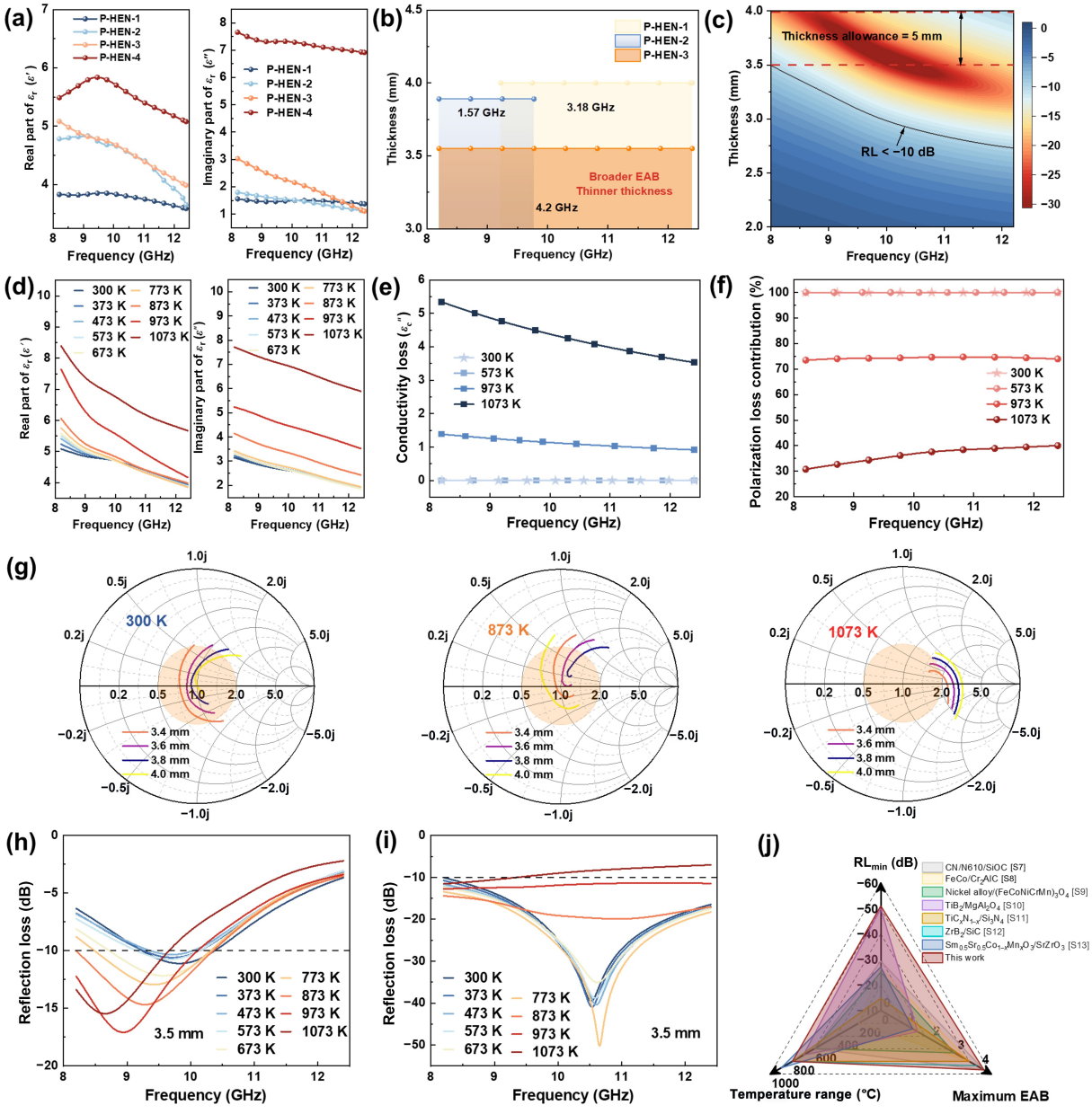

Figure 4 (a) ε' and ε'' and (b) EAB for P-HEN with different $(FeNiCoAl)_3O_4$ nanocrystal contents. (c) 2D RL mapping below −10 dB for P-HEN-3. (d) Temperature-dependent ε' and ε'' of P-HEN-3. Temperature-dependent (e) conductive loss component and (f) polarization loss contribution of P-HEN-3. (g) Smith charts of P-HEN-3 at different temperatures and different thicknesses. Temperature-dependent RL of (h) P-HEN-2 and (i) P-HEN-3 with a thickness of 3.5 mm. (j) Comparison of the EMW absorbing performance of P-HEN with other materials (Table S1 in the ESM).

gives rise to a pronounced interfacial polarization response. Under high-temperature conditions, the quasi-percolation network formed by semiconducting nanocrystals significantly introduces conductive loss. Consequently, the marked increase in conductive loss at elevated temperatures leads to a noticeable decrease in the contribution of polarization loss, thereby revealing a transition in the dominant dielectric loss mechanism.

Furthermore, Cole–Cole plots constructed at different temperatures based on Debye relaxation theory were used to analyze the polarization-relaxation behavior (Fig. S13 in the ESM). Typically, the $\varepsilon' - \varepsilon''$ plot exhibits one or more semicircles (Cole–Cole semicircles), where each semicircle corresponds to a Debye relaxation process. As shown, the irregular Cole–Cole semicircle features are well preserved upon increasing temperature, suggesting the presence of multiple relaxation processes, which mainly originate from the localized dipolar polarization introduced by the nanocrystals and the associated interfacial-polarization effects. Meanwhile, the conduction loss arising from the transport network built by the nanocrystals couples with the dielectric-loss behavior. Consequently, P-HEN maintains a stable dielectric-loss capability over a broad temperature range. Beyond the loss mechanisms, the Smith chart shows that the optimal matching-thickness curves of P-HEN-3 across the wide temperature window all pass through the central region, indicating that P-HEN-3 preserves good impedance-matching characteristics at high temperatures (Fig. 4(g)). Subsequently, the EMW absorption performance of P-HEN was calculated across a broad temperature range from 300 to 1073 K (Figs. 4(h) and 4(i), and Figs. S14 and S15 in the ESM). Among

them, P-HEN-3 exhibits outstanding wide-temperature-range EMW absorption, maintaining RL values below −10 dB throughout the entire X band within the temperature range of 300 to 973 K, highlighting its potential for high-temperature electromagnetic protection. The comparison of the normalized impedance matching modulus of P-HEN-2 and P-HEN-3 at different temperatures reveals that the temperature evolution of the permittivity leads to the deterioration of impedance matching in P-HEN-3 under extremely high-temperature conditions (Fig. S16 in the ESM). Nevertheless, owing to the excellent dielectric tunability of the dielectric network formed by the $(FeNiCoAl)_3O_4$ nanocrystals, a balance can be achieved between dielectric evolution with temperature and impedance matching over a wide temperature range. As a result, this balance endows P-HEN-3 with significant advantages over other high-temperature EMW absorbing materials in terms of RL_{min}, EAB, and operational temperature range (Fig. 4(j) and Table S1 in the ESM).

3.3 Compatibility of radar stealth and high-temperature thermal protection

At present, high-temperature stealth technology is of profound strategic significance for enhancing the survivability of advanced platforms operating under hypersonic flight and extreme service conditions, and it has become a pivotal research direction for promoting defense modernization and strengthening overall military capability. To evaluate the radar cross section (RCS) suppression efficacy of the P-HEN-3 as a coating material, its RCS reduction performance is systematically validated using computer simulation technology (CST) electromagnetic simulations. In the simulations, a perfect electric conductor (PEC) plate model with dimensions of 180 mm × 180 mm and a thickness of 3.5 mm is first established, and an P-HEN-3 coating is introduced onto its surface to emulate the scattering characteristics after coating (Fig. 5(a)). As shown in Fig. 5(b), when the plane-wave incidence angle is set to 0°, the P-HEN-3 exhibits a pronounced RCS reduction in the X-band, indicating its potential for electromagnetic stealth as a coating material. Moreover, when the PW incidence angle varies, the composite still maintains a low RCS level, suggesting that the P-HEN-3 coating can effectively suppress scattering signals within a certain angular range, thereby improving resistance against multi-aspect radar detection. In addition, Fig. 5(c) presents the two-dimensional RCS distributions at different $(FeNiCoAl)_3O_4$ nanocrystal loading concentrations. Notably, the P-HEN-3 achieves an evident RCS reduction, demonstrating excellent scattering suppression capability.

In extreme service scenarios, whether a coating can retain its RCS reduction capability at elevated temperatures constitutes one of the central challenges for realizing high-temperature stealth. Accordingly, under typical frequency conditions (10 GHz), a

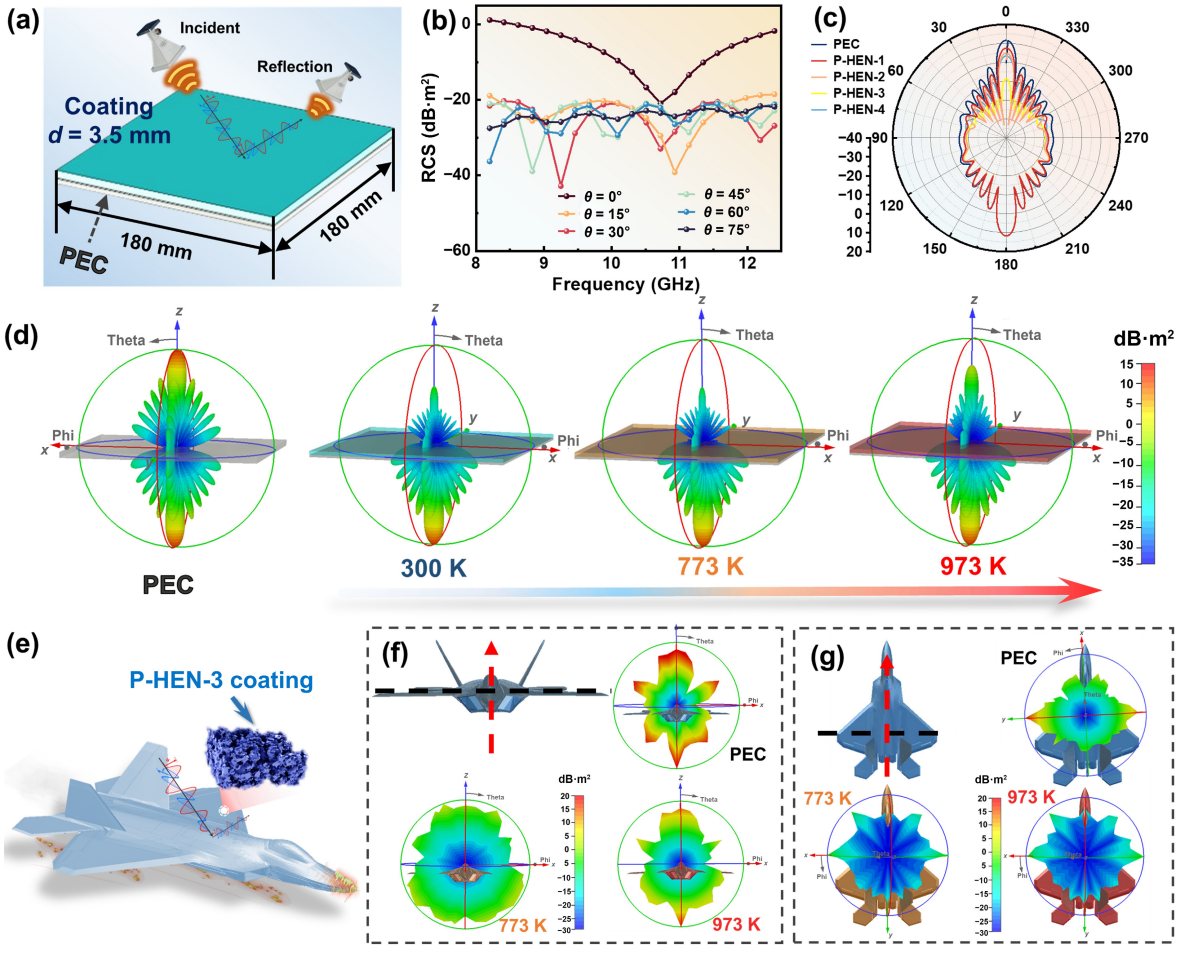

Figure 5 (a) Rectangle PEC substrate covered with absorber. (b) RCS simulated curves of P-HEN-3 under different plane wave angles. (c) RCS polar system for P-HEN with different $(FeNiCoAl)_3O_4$ nanocrystal contents. (d) 3D radar scattering signals of the P-HEN-3 at different temperatures. (e) Schematic diagram of the model coated with the P-HEN-3. (f) The front view and (g) top view of the 3D radar scattering signals of the model after coating P-HEN-3.

comparative evaluation is conducted on the RCS suppression performance of the P-HEN-3 coating at 300, 773, and 973 K. As shown in Fig. 5(d), even in high-temperature environments, the coating still sustains highly efficient RCS reduction, evidencing favorable high-temperature EMW absorption and stealth stability. To further verify the stealth applicability and conformability of the P-HEN-3 coating under a geometry closer to practical platforms, an F22 aircraft model is constructed to simulate the high-temperature stealth performance after coating (Fig. 5(e)). The front-view results show that the uncoated model exhibits strong scattering responses in prominent feature regions such as the wings and nose (Fig. 5(f)). After applying the P-HEN-3 coating, the high-scattering signatures at sharp structural features are markedly attenuated, and the RCS distribution becomes smoother. Meanwhile, the scattering levels across other regions of the airframe are also reduced overall, and a favorable RCS suppression effect is likewise maintained under high-temperature conditions. The top-view results further demonstrate that the RCS of the F22 model coated with P-HEN-3 is significantly reduced (Fig. 5(g)). Therefore, the P-HEN-3, as a coating material, is capable of continuously achieving effective RCS suppression under both ambient and high-temperature conditions, highlighting its outstanding high-temperature stealth performance and engineering application potential.

In the realm of high-temperature stealth applications, the dielectric stability of materials is contingent not merely upon their intrinsic electromagnetic attributes but is, more critically, governed by their structural integrity within extreme thermal environments. Consequently, exceptional ablation resistance and thermal protection efficacy constitute the prerequisites for guaranteeing the service reliability of high-temperature stealth materials. From the perspective of microstructural design, benefiting from the soft-template induction effect of melamine foam, the P-HEN-3 has successfully constructed a hierarchically interconnected microporous network architecture. This unique porous configuration effectively obstructs phonon transmission pathways, significantly reducing the contribution of solid-phase thermal conduction and endowing the material with superior thermal insulation potential. As illustrated in Fig. 6(a), all samples filled with $(FeNiCoAl)_3O_4$ nanocrystals maintain highly porous characteristics, wherein the P-HEN-3 exhibits an average pore size of approximately 81.7 μm. Characterization results of temperature-dependent thermal conductivity further corroborate the advantages of this microstructure (Fig. 6(b)). Measurements demonstrate that the P-HEN-3 exhibits exceptional low thermal conductivity, being only 0.419 W/(m·K) at 300 K. Even at an elevated temperature of 1273 K, where thermal radiation is significantly intensified, its thermal conductivity is maintained at a low level of 1.367 W/(m·K). This low thermal transmission rate effectively suppresses the diffusion of heat flux within the material, providing theoretical support for its application as thermal barrier coatings or structural components.

To evaluate its practical thermal protection efficacy, a dynamic thermal response test was established (Fig. 6(c)). As the ambient temperature increases continuously to 850 °C, benefiting from the internal thermal resistance, the P-HEN-3 exhibits a significant temperature hysteresis effect. After prolonged heating for 5000 s, its surface temperature reaches only 372.7 °C, confirming its superior thermal insulation shielding performance. Furthermore, a transient ablation assessment under extreme conditions was conducted on the P-HEN-3 using oxyacetylene ablation test system to verify its thermo-mechanical stability under authentic operating conditions (Fig. 6(d) and Table S2 in the ESM). Upon exposure to a high-temperature airflow impact at approximately 2400 KW/m^2 for 20 s, the sample demonstrates excellent structural resistance. Despite undergoing severe thermal shock and airflow shear, the macroscopic morphology of the sample remains fundamentally intact, without the occurrence of catastrophic pulverization or disintegration. Quantitative analysis reveals that the mass ablation rate and linear ablation rate of P-HEN-3 are 16.33 mg/s and 19.50 μm/s, respectively, demonstrating excellent ablation resistance (Table S3 in the ESM). The temperature monitoring of the surface indicates that P-HEN-3 was exposed to a high-temperature and high-speed gas flow of up to 2100 °C. and due to the occurrence of the melting process, the surface roughness further decreased to 20.69 μm (Fig. 6(e)). This superior ablation resistance mechanism is primarily attributed to two factors: Firstly, the high-porosity structure acts as a thermal buffer layer to effectively dissipate thermal stress; secondly, the SiOCN ceramic matrix likely generates a dense silica-based protective film in situ at elevated temperatures, retarding the further oxidative decomposition of the internal matrix. Consequently, by virtue of its unique microscopic porous architecture and the intrinsic thermal resistance of the ceramic matrix, the P-HEN-3 achieves exceptional ablation resistance and efficient thermal protection functionality, thereby providing a prerequisite for high-temperature stealth technology.

The corresponding mechanism of high-temperature EMW absorption and thermal protection of P-HEN is schematically shown in Fig. 6(f). From the perspective of radar stealth mechanisms, the $(FeNiCoAl)_3O_4$ nanocrystals act as dielectric-activation units, markedly enhancing the dissipative dielectric response of the composite. First, the random occupation of high-entropy multimetal cations within the spinel lattice induces pronounced local charge density fluctuations and potential well distributions at the atomic scale, thereby forming stable polarization-heterogeneous regions. The heterogeneous charge environment enhances dipolar polarization and relaxation losses, while dielectric and band-structure mismatches at the nanocrystal/SiOCN interfaces induce interfacial polarization via carrier accumulation-release processes, jointly amplifying dielectric loss [44, 45]. From the perspective of high-temperature thermal protection, the high porosity and hierarchical pore architecture introduced by the soft-template strategy markedly reduce the effective thermal conductivity by disrupting continuous phonon transport through abundant solid–gas interfaces and tortuous heat-flow pathways, while simultaneously weakening radiative heat transfer via multiple reflections. More importantly, the SiOCN polymer-derived ceramic matrix provides excellent high-temperature structural stability and resistance to oxidation and thermal shock, maintaining skeletal integrity and buffering thermal stresses to ensure morphological and functional stability under extreme thermal conditions. Therefore, the combination of high-porosity thermal insulation effects and the high-temperature structural support provided by the SiOCN matrix constitutes the fundamental basis for the superior thermal protection performance of the P-HEN, which, when coupled with multi-mechanism dielectric dissipation, enables the simultaneous compatibility of electromagnetic stealth and thermal protection under high-temperature conditions.

4 Conclusion

A melamine-foam soft-templating strategy is employed to incorporate multiscale, discretely distributed $(FeNiCoAl)_3O_4$ high-entropy spinel nanocrystals into a SiOCN ceramic matrix, thereby

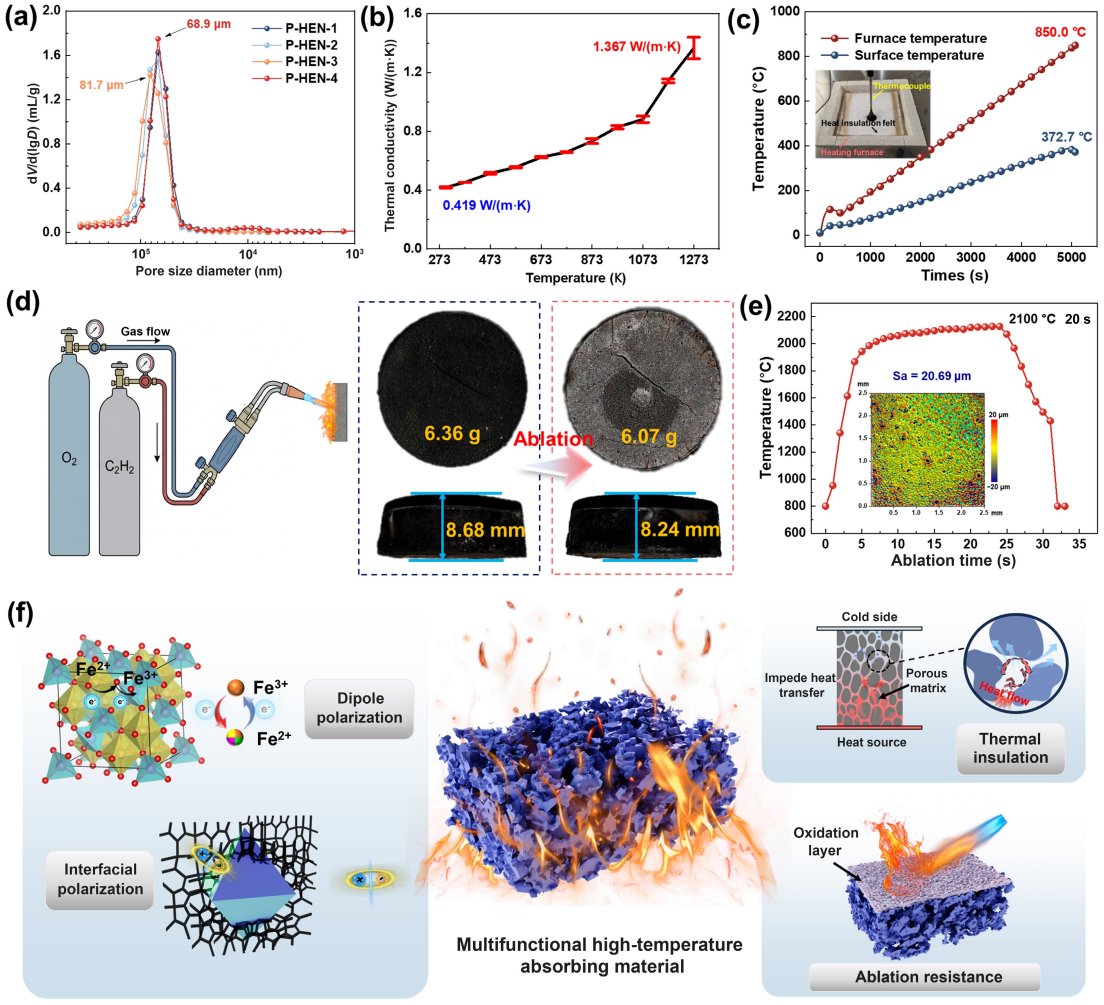

Figure 6 (a) Pore size distributions of P-HEN. (b) Temperature-dependence thermal conductivity and (c) thermal insulation performance of P-HEN-3. (d) Comparison of P-HEN-3 before and after oxyacetylene ablation. (e) Surface temperature during ablation and CLSM morphology of the surface after ablation. (f) Schematic diagram of the high-temperature EMW loss and thermal protection mechanism of P-HEN.

achieving synergistic compatibility between EMW absorption and high-temperature thermal protection. The continuous SiOCN covalent network provides confinement and protective effects, enabling persistent dielectric loss of the $(FeNiCoAl)_3O_4$ nanocrystals even at elevated temperatures. This design leverages the synergistic interplay of conduction loss and polarization loss across a broad temperature range, resulting outstanding high-temperature EMW absorption performance. The composite materials effective operates across the entire X-band from 300 to 973 K, demonstrating excellent thermal-insulation capability and ablation resistance. This work provides a rational design strategy for developing of high-temperature EMW absorbers for extreme environments.

Electronic Supplementary Material: Supplementary material (supplementary notes and figures) is available in the online version of this article at https://doi.org/10.26599/NR.2026.94908670.

Data availability

All data needed to support the conclusions in the paper are presented in the manuscript and the Electronic Supplementary Material. Additional data related to this paper may be requested from the corresponding author upon request.

Acknowledgements

This work was supported by The Youth Innovation Team of Shaanxi Universities and The Innovation and Entrepreneurship Team of Special Support Program for 'Sanqin' Talent, Special Support Program for High-level Talents of Shaanxi Province (No. 2020-44), Natural Science Basic Research Program of Shaanxi Province (Nos. 2025JC-YBQN-665 and 2024JC-YBMS-291), the National Natural Science Foundation of China (Nos. 52225104 and 525B2009), and the open research fund of Suzhou Laboratory (No. SZLAB-1508-2025-TS029).

Declaration of competing interest

All the contributing authors report no conflict of interests in this work.

Author contribution statement

W. C. W. designed the experiments and wrote the manuscript. W. C. W., J. H., Q. Q. W., Q. G., C. Q. G., X. W. Y., and S. Y. performed characterizations. G. L., L. Y. W., and R. B. W. supervised the project and revised the manuscript. All authors discussed the results and commented on the manuscript.

Use of AI statement

None.

References

[1] Li, Y.; Qing, Y. C.; Li, W.; Ma, C.; Bai, Z. Y.; Shao, G.; Wang, H. L.; Huang, M.; Liu, X. H.; Fan, B. B. Harnessing carbon-containing materials for next-generation high-temperature electromagnetic wave absorbers. *Carbon Energy* **2026**, *8*, e70118.

[2] Wang, W. C.; Wang, L. Y.; Huang, J.; Gu, Q.; Lu, Y. Y.; Ge, C. Q.; Liu, G. Leveraging counteractive temperature-dependent resistivity among components for temperature-insensitive electromagnetic characteristics in lightweight SiOCN ceramics. *Chem. Eng. J.* **2025**, *513*, 163011.

[3] Song, Y.; Liu, P.; Zhou, R.; Zhu, R. Q.; Kong, J. SiBNC$_x$ ceramics derived from single source polymeric precursor with controllable carbon structures for highly efficient electromagnetic wave absorption at high temperature. *Carbon* **2022**, *188*, 12–24.

[4] Lv, H. L.; Yang, Z. H.; Pan, H. G.; Wu, R. B. Electromagnetic absorption materials: Current progress and new frontiers. *Prog. Mater. Sci.* **2022**, *127*, 100946.

[5] Yang, Z. H.; Lv, H. L.; Wu, R. B. Rational construction of graphene oxide with MOF-derived porous NiFe@C nanocubes for high-performance microwave attenuation. *Nano Res.* **2016**, *9*, 3671–3682.

[6] Wang, Q. Q.; Liu, D.; Zhou, J.; Liu, G.; Wang, L. Y.; Wu, R. B. Intelligentization of electromagnetic functional materials: From design to applications. *Adv. Mater*., in press, DOI: 10.1002/adma.202510212.

[7] Zhang, C.; Wang, X. A novel high-temperature FeSiAl/CaO–B_2O_3–SiO_2 microwave absorption coating prepared via atmospheric plasma spraying. *Ceram. Int.* **2024**, *50*, 29044–29055.

[8] Xia, Q. S.; Han, Z.; Zhang, Z. C.; Huang, Z. Y.; Wang, X. T.; Chang, J.; Chen, Q. G.; Chen, M. H. High temperature microwave absorbing materials. *J. Mater. Chem. C* **2023**, *11*, 4552–4569.

[9] Wang, W. C.; Liu, G.; Wang, L. Y.; Ge, C. Q.; Wang, L.; Wang, B.; Huang, J. Temperature-dependent dielectric and wide-temperature-range microwave absorption properties of $La_{0.8}Sr_{0.2}MnO_3$/Al_2O_3-13%TiO_2 coatings. *Ceram. Int.* **2023**, *49*, 34595–34602.

[10] Zhang, H.; Deng, G.; Sun, X.; Yan, L.; Han, G. Y.; Cui, Z. R.; Zhang, Y.; Zhang, Y. Y.; Xie, K. B.; Yu, R. H. et al. Interface chemical welding by nanoparticles endow ceramic aerogels with broad-temperature microwave absorption and thermal insulation. *Adv. Funct. Mater*. **2026**, *36*, e24866.

[11] Wang, Z. X.; Yang, T.; Zhou, L. L.; Hou, X. M.; Fang, Z.; Hou, Y. L. Current progress and challenges of electromagnetic wave absorbing materials at high temperature. *Adv. Sci.* **2025**, *12*, e04286.

[12] Wang, W. C.; Wang, L. Y.; Liu, G.; Ge, C. Q.; Wang, L.; Wang, B.; Huang, J. Temperature-dependent dielectric properties and high-temperature microwave absorption performance of Ti_3SiC_2/Al_2O_3-13%TiO_2 coatings. *J. Eur. Ceram. Soc.* **2024**, *44*, 254–260.

[13] Yu, Z. J.; Zhu, Q. K.; Li, F.; Chen, T.; Du, H. Z. Single-source-precursor derived multicomponent CNTs/Fe_3Si/Fe/SiOCN ceramic nanocomposites: Microstructural evolution and excellent electromagnetic wave absorbing properties. *J. Mater. Chem. C* **2022**, *10*, 6252–6262.

[14] Wang, W. C.; Wang, L. Y.; Huang, J.; Gu, Q.; Lu, Y. Y.; Ge, C. Q.; Qing, Y.; Liu, G. Multi-heterointerface lightweight ceramics achieving temperature-insensitive dielectric properties for high-temperature electromagnetic wave effective absorption. *J. Adv. Ceram.* **2025**, *14*, 9221135.

[15] Geng, T. B.; Yu, G. Y.; Shao, G. F.; Huang, X. G. Enhanced electromagnetic wave absorption properties of ZIF-67 modified polymer-derived SiCN ceramics by *in situ* construction of multiple heterointerfaces. *Rare Met.* **2023**, *42*, 1635–1644.

[16] Huang, J.; Wang, L. Y.; Wang, B.; Wang, W. C.; Ge, C. Q.; Wang, X. L.; Hu, Z. F.; Liu, G.; Che, R. C. Amide bond-induced charge-directed transport: Constructing capture-release networks for enhanced electromagnetic wave attenuation. *Adv. Funct. Mater.* **2026**, *36*, e22909.

[17] Yu, G. Y.; Shao, G. F.; Xu, Z. L.; Chen, Y.; Huang, X. G. Hierarchical interface-engineered magnetic graphene-SiCN aerogels via a stepwise confinement strategy for low-frequency and broadband microwave absorption. *J. Adv. Ceram.* **2025**, *14*, 9221187.

[18] Huang, J.; Wang, L. Y.; Wu, R. B.; Wang, W. C.; Ge, C. Q.; Yang, H. K.; Tang, X.; Jiao, W. Y.; Liu, G.; Wang, B. Coupling of 0D/1D grain boundaries inducing extreme charge rearrangement/magnetic resonance for ultrabroadband electromagnetic wave absorption. *Carbon Energy*, in press, DOI: 10.1002/cey2.70126.

[19] Huang, J.; Hu, L. J.; Wang, L. Y.; Wang, W. C.; Ge, C. Q.; Wang, L.; Chen, M. Z.; Wu, R. B.; Liu, G.; Wang, B. Constructing Pb–O bonds to trigger efficient cross-scale charge transfer for high-performance electromagnetic wave absorption and multicolor conversion. *Chem. Eng. J.* **2025**, *504*, 159004.

[20] Liu, R. L.; Jiang, X. M.; Ni, C.; Wang, B. L.; Hou, C. X.; Yang, X. Y.; Zhang, Y. P.; Du, W.; Xie, X. B. Multi-shell layer heterostructure construction of Co/$Ni_3ZnC_{0.7}$/C composite with built-in electric field for efficient electromagnetic response. *Adv. Funct. Mater*. **2026**, *36*, e23317.

[21] Bao, Y. F.; Liu, Y.; Wang, W. R.; Qi, X. Q.; Jia, Z. Q.; Guo, S. Y. Thermal-driven structure-phase cooperative evolution of magnetic micro-flower on biomass-derived carbon for exceptional microwave absorption and radar-infrared stealth. *Small* **2026**, *22*, e12704.

[22] Shu, Y.; Zhao, T. K.; Jia, W. Y.; Yang, L.; Li, X. H.; Feng, G. Y.; Li, Y. T.; Luo, F. A crosslinked coral-like Co@CoO/RGO nanohybrid structure with good electromagnetic wave absorption performance. *J. Colloid Interface Sci.* **2023**, *642*, 393–407.

[23] Xiong, X. H.; Liu, Z. W.; Zhang, R. X.; Yang, L. T.; Liang, G. S.; Zhou, X. D.; Li, B. X.; Zhang, H. B.; Lv, H. L.; Che, R. C. Atomic-level electric polarization in entropy-driven perovskites for boosting dielectric response. *Adv. Mater.* **2025**, *37*, 2415351.

[24] Guo, P. F.; Liu, D.; Wang, Q. Q.; Chen, P.; Yang, H. W.; Zhang, M. C.; Zheng, C.; Jiang, L.; Pan, H. G.; Wu, R. B. Balancing the surface reconstruction of spinel oxides for efficient oxygen evolution reaction. *Nano Lett.* **2025**, *25*, 10209–10217.

[25] Singha, D. K.; Ping, T. P.; Jena, B. K. Modulation of the proportion of mixed metals in spinel-type oxide $Ni_xCo_{3-x}O_4$ (x = 0–1) derived from a metal-organic framework for enhanced oxygen evolution reaction. *ACS Appl. Energy Mater.* **2023**, *6*, 9963–9974.

[26] Guo, P. F.; Shi, L. X.; Liu, D.; Wang, X. Q.; Gao, F.; Ha, Y.; Yin, J.; Liu, M.; Pan, H. G.; Wu, R. B. Fe-doping-induced cation substitution and anion vacancies promoting Co_3O_4 hexagonal nanosheets for efficient overall water splitting. *Mater. Today Catal.* **2023**, *1*, 100002.

[27] Wei, S.; Sun, T. X.; Ma, C. C.; Gao, H.; Zhao, Z. P.; Feng, H. M.; Li, W.; Chen, S. G. Improved interfacial interactions by core-shell $CoFe_2O_4$@SiO_2 composites to enhance the ability of corrosion resistance and electromagnetic wave absorption. *Small* **2024**, *20*, 2405814.

[28] Liu, G. J.; Wang, L.; Zhang, H.; Du, Z. Y.; Zhou, X. Y.; Wang, K. K.; Sun, Y. M.; Gao, S. M. Cage-structured $CoFe_2O_4$@CNTs from Fe–Co-MOF confined growth in CNTs for high electromagnetic wave absorption performances. *Compos. Commun.* **2021**, *27*, 100910.

[29] Shi, B.; Liang, H. S.; Xie, Z. J.; Chang, Q.; Wu, H. J. Dielectric loss enhancement induced by the microstructure of $CoFe_2O_4$ foam to realize broadband electromagnetic wave absorption. *Int. J. Miner. Metall. Mater.* **2023**, *30*, 1388–1397.

[30] Ye, Z. L.; Xia, Y. C.; Luo, R. Y.; Yang, H. Y.; Liu, Y.; Zheng, K.; Ye, Z. H.; Yang, X. T.; Sun, S. Y.; Lei, B. Y. Effect of $NiFe_2O_4$ filler on the wave-absorbing properties of PIP-SiC/SiCN composites. *Chem. Eng. J.* **2025**, *521*, 166976.

[31] Liu, D.; Guo, P. F.; Pan, H. G.; Wu, R. B. Emerging high-entropy

compounds for electrochemical energy storage and conversion. *Prog. Mater. Sci.* **2024**, *145*, 101300.

[32] Tao, J. Q.; Yan, Y.; Zhou, J. T.; Wang, J.; Chen, P.; Tan, R. Y.; Xu, L. L.; Zhu, H. B.; Zhu, W. H.; Huang, H. X. et al. Anionic high-entropy doping engineering for electromagnetic wave absorption. *Nat. Commun.* **2025**, *16*, 3163.

[33] Hoch, C. Syntheses and crystal structures of solvate complexes of alkaline earth and lanthanoid metal iodides with *N,N*-dimethylformamide. *Z. Kristallogr.-Cryst. Mater.* **2020**, *235*, 401–411.

[34] Li, W. H.; Sunarso, J.; Yang, Y.; Chen, Y. J.; Ge, C. L.; Wang, W.; Guo, Y.; Ran, R.; Zhou, W. Strategies for improving oxygen ionic conducting in perovskite oxides and their practical applications. *Energy Rev.* **2024**, *3*, 100085.

[35] Boukha, Z.; Jiménez-González, C.; de Rivas, B.; González-Velasco, J. R.; Gutiérrez-Ortiz, J. I.; López-Fonseca, R. Synthesis, characterisation and performance evaluation of spinel-derived Ni/Al_2O_3 catalysts for various methane reforming reactions. *Appl. Catal. B: Environ.* **2014**, *158–159*, 190–201.

[36] Mande, V. K.; Borade, R. B.; Raut, V. B.; Pawar, R. P. Rietveld refinement and cation distribution of Zn–Al substituted $NiFe_2O_4$ ferrite nanoparticles. *J. Magn. Magn. Mater.* **2024**, *596*, 171908.

[37] Yang, N.; Lu, K. Phase content prediction in polymer-derived ceramics with metal additives. *J. Am. Ceram. Soc.* **2021**, *104*, 5379–5391.

[38] Liu, Y. Q.; Yang, B. B.; Lan, S.; Zhou, Z. F.; Dou, L.; Nan, C. W.; Lin, Y. H. Harnessing local inhomogeneity for enhanced dielectric energy storage. *Nat. Commun.* **2025**, *16*, 6236.

[39] Lizarbe, A. J.; Major, G. H.; Fernandez, V.; Fairley, N.; Linford, M. R. Insight note: X-ray photoelectron spectroscopy (XPS) peak fitting of the Al 2p peak from electrically isolated aluminum foil with an oxide layer. *Surf. Interface Anal.* **2023**, *55*, 651–657.

[40] Tao, N.; Liu, J. D.; Xu, Y. J.; Feng, Y. C.; Wang, Y. Y.; Liu, W. R.; Wang, H. F.; Lv, J. H. Highly selective and stable ZrO_2–Al_2O_3 for synthesis of dimethyl carbonate in reactive distillation. *Chem. Pap.* **2020**, *74*, 3503–3515.

[41] Chen, Z. L.; Wu, R. B.; Liu, Y.; Ha, Y.; Guo, Y. H.; Sun, D. L.; Liu, M.; Fang, F. Ultrafine Co nanoparticles encapsulated in carbon-nanotubes-grafted graphene sheets as advanced electrocatalysts for the hydrogen evolution reaction. *Adv. Mater.* **2018**, *30*, 1802011.

[42] Zhou, Y.; Zhou, B. L.; Jin, S. Y.; Luo, Z.; Qian, W.; Guo, J. N.; Li, B. W.; Zu, H. R.; Song, R. G.; He, D. P. Highly reliable and ultra-wideband metamaterial absorber based on graphene-assembled films for extremes. *Carbon* **2024**, *229*, 119534.

[43] Su, X. G.; Wang, J.; Liu, T.; Zhang, Y.; Liu, Y. N.; Zhang, B.; Liu, Y. Q.; Wu, H. J.; Xu, H. X. Controllable atomic migration in microstructures and defects for electromagnetic wave absorption enhancement. *Adv. Funct. Mater.* **2024**, *34*, 2403397.

[44] Chen, P. F.; Yang, X. R.; Chang, Y. F.; Qian, W.; Fu, H. Q.; Xu, W. X.; Ren, L.; Wang, Z.; Zu, H. R.; Wang, D. S. et al. Superior microwave shielding modulation based on rapidly prepared graphene metasurface. *Natl. Sci. Rev.* **2025**, *12*, nwaf395.

[45] Yu, G. Y.; Shao, G. F.; Xu, R. P.; Chen, Y.; Zhu, X. H.; Huang, X. G. Metal-organic framework-manipulated dielectric genes inside silicon carbonitride toward tunable electromagnetic wave absorption. *Small* **2023**, *19*, 2304694.